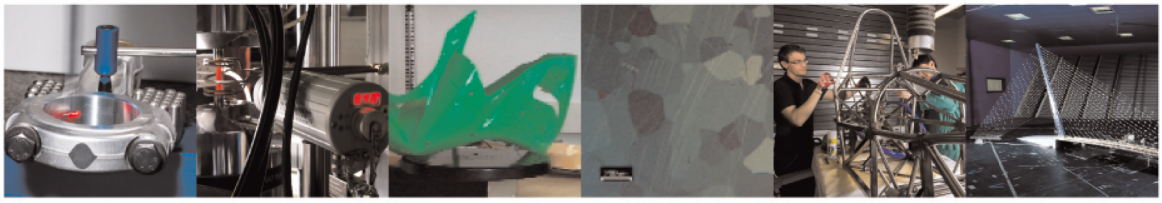

On crack tip localisation in quasi-statically loaded, adhesively bonded double cantilever beam specimens by acoustic emission

R. A. A. Lima, M. Drobiazko, A. Bernasconi, M. Carboni

This is a post-peer-review, pre-copyedit version of an article published in Theoretical and Applied Fracture Mechanics. The final authenticated version is available online at https://doi.org/10.1016/j.tafmec.2022.103286

DIPARTIMENTO DI MECCANICA ■ POLITECNICO DI MILANO
via G. La Masa, 1 ■ 20156 Milano ■ EMAIL (PEC): pecmecc@cert.polimi.it
http://www.mecc.polimi.it
Rev. 0

On crack tip localisation in quasi-statically loaded, adhesively bonded double cantilever beam specimens by acoustic emission

R. A. A. Lima, M. Drobiazko, A. Bernasconi, M. Carboni[1]

Dept. Mechanical Engineering, Politecnico di Milano, Milan, Italy

The feasibility of acoustic emission structural health monitoring to detect, localise and monitor crack propagation during quasi-static mode I loading of adhesively bonded joints was studied. Unsupervised artificial intelligence pattern recognition methods (Self-Organised maps and K-means) were used to classify acoustic emission raw data as either background noise or relevant information. After that, three different time-of-arrival picking algorithms were considered and implemented to determine the acoustic emission source's location, and their accuracy was discussed. Localised acoustic emission events were divided into well-defined groups with different energy levels and compared to Digital Image Correlation and visual evaluation results. It was possible to conclude that the highest energetic group allows the assessment of the onset of plasticisation ahead of the crack-tip within the studied adhesive, bringing novel standpoints to the use of acoustic emission as a structural health monitoring method for adhesively bonded joints.

Keywords: adhesively bonded joints, crack-tip location, acoustic emission, digital image correlation.

[1] Corresponding author: Tel.: +39-02-23998253, Fax: +39-02-23998202, e-mail: michele.carboni@polimi.it (M. Carboni).

1. INTRODUCTION

The use of adhesive joints in the aerospace, automotive, and naval industries has increased in recent years due to their main advantages: low weight, uniform stress distribution, multi-materials joining, and higher design flexibility compared with traditional mechanical joining solutions [1], [2]. Nevertheless, adhesively bonded joints are vulnerable to environmental and ageing actions, being difficult to ensure their safety and reliability during their in-service life [3].

To guarantee the use of adhesive joints in primary structures and avoid premature failures, Non-Destructive Testing (NDT) and Structural Health Monitoring (SHM) methods have been developed and are commonly applied [4], [5]. The main advantage of SHM methods, compared to NDT techniques, is the possibility of real-time or on-demand monitoring of in-service structures and of identifying, locating, and quantifying the damaged zones in larger assembled structures [6], [7]. In addition, an operational history of the monitored systems is created, allowing a maintenance plan based on the structures' actual state instead of predefined service interruptions, and, consequently, a reduction of their maintenance costs can be observed [8], [9].

Today, the main physical phenomena characterising the available SHM methods and approaches are [10], [11]:

- elastic waves: this method actively produces ultrasonic elastic waves, often ultrasonic guided waves, whose unexpected propagating behaviour through a component might indicate whether a reflecting surface or an internal damage are present. Elastic waves' speed variations can suggest if a debonded area is present in adhesively bonded joints, for example [12]–[14];
- modal data: this is an SHM method based on the identification of changes in the modal frequencies or other non-linear phenomena, such as self-modulation or hysteresis and, also, reduction of structural stiffness, when a component presents damage [15], [16];

- static parameters: this method is based on assessing changes in the strain or displacement fields during damage development in the monitored components, using punctual (e.g. strain gauges and optical fibres with Fibre-Bragg Gratings) or distributed (e.g. conventional optical fibres using Optical Backscatter Reflectometry method) sensors [17]–[21]. This method can identify the crack-tip position within brittle adhesives and the onset of plasticisation in some toughened adhesives [22];
- electro-mechanical impedance: this method is based on the changes in the component's total electro-mechanical impedance due to defects and damage. Carbon nanotubes, for example, are being massively implemented as damage sensors of adhesively bonded joints and composite materials since their electrical resistance variates under mechanical stresses and during damage development [6], [23];
- acoustic emission (AE): this passive method assesses ultrasonic elastic waves produced when the structure's strain energy is spontaneously released due to irreversible straining or damage [24][25]. This energy-releasing phenomenon is similar to a small-scale earthquake within the material, where elastic waves are produced suddenly after deformation or damage initiation and propagation. Once these waves are assessed by using specific sensors (i.e. piezoelectric and wide-band transducers), it is possible to identify the wave's features (energy, counts, duration, amplitude, frequency and others) and to correlate them with the damage mechanisms happening in the monitored material [5], [25], [34], [26]–[33].

AE appears to be a promising method for SHM of adhesively bonded joints. Its main advantages include identifying and localising different damage mechanisms in the substrates (e.g., in the case of composite materials, pull-out, matrix-cracking, delamination and ply-fragmentation) [13]–[21] and within the adhesive layer by triangulation of the AE source's position, with great accuracy, from damage initiation to final failure, as described in the literature review by M. Saeedifar and D. Zarouchas [35]. In addition, the adopted sensors are often not embedded into the structure and are less bulky, so being easily replaced in case of operational issues.

Since the AE method is very sensitive and, consequently, allows assessing a massive amount of data, an efficient post-processing method based on big-data analytics is often necessary to divide and separate the AE signals related to background noise from those related to damage mechanisms. Generally, time-domain, frequency-domain and time-frequency processing tools are widely used in the literature to analyse AE signal's features [24], [26], [28], [36]–[38]. However, recently, supervised and unsupervised Artificial Neural Networks (ANN) as Self-Organising Maps (SOM), Principal Component Analysis (PCA) and K-means are becoming popular approaches to classify AE signals and to identify damage mechanisms, for example in composite materials [25], [33], [39]–[43], due to their automatisation and the possibility to analyse simultaneously different features of a big data, increasing the repeatability of the results.

Few studies [44]–[52] are dedicated to using AE to monitor crack propagation in adhesively bonded joints and to correlate the waveform's features with the damage mechanisms within the bondline (cohesive or adhesive failures). For example, S. Teixeira de Freitas et al. [16] distinguished cohesive from adhesive failures in adhesively bonded joints under quasi-static mode I loading conditions by different energy levels of the AE hits. Furthermore, the most energetic AE energy groups were correlated to cohesive failures since its fracture process is mainly controlled by plastic deformations ahead of the crack-tip.

In addition, the comparison between AE responses of different adhesive's types (ductile and brittle) has not been studied extensively enough. J. Manterola *et al*. [50] presented one of the few works investigating this influence. They observed that, for the performed quasi-static mode I tests, AE signals corresponded to the sample's maximum normal stress, this region for the ductile adhesive did not represent the crack tip since its fracture process zone presented a significant size. On the other hand, the position coincided with the crack-tip position determined by visual inspection for the brittle adhesive.

Nevertheless, to the best of the author's knowledge, it is still difficult to establish whether the AE events produced within joints bonded with ductile adhesives are only related to the samples' region of maximum normal stress or whether they may also represent the onset

of plasticisation or indicate different damage modes (e.g., void coalescence and cavitation). Therefore, machine learning algorithms can be a valuable tool to discriminate better the AE hits using multivariate (high-dimensional) analysis of different AE features since they are interdependent and can be associated with various damage mechanisms [53].

So, the present research work aims to localise the crack-tip, by AE monitoring, within Double Cantilever Beam (DCB) joints bonded with a ductile adhesive. Specifically, a quasi-static mode I loading condition, realised by the DCB configuration, was selected since it is a well-known scenario, and high-strength steel was chosen as substrates' material to avoid competition between adhesive/adherent failure mechanisms that could complicate the interpretation of the results.

A particular focus is also given to the methodological approach to classifying AE raw data using a self-organising map and K-means algorithm as a non-supervised ANN and dividing them between AE waves related to background noise and damage propagation. Three time-of-arrival (ToA) picker algorithms (Akaike Information criteria, Threshold Adopted to Maximum Amplitude Signal, and Baer and Kradolfer [54], [55]) were analysed and their effectiveness to localise sources of acoustic emissions were compared. In addition, visual evaluation and Digital Image Correlation (DIC) measurements were also performed to support the discussion of the AE results since, combining both methods, it is possible to estimate the length of the adhesive's Fracture Process Zone (FPZ) [22], [56].

2. EXPERIMENTAL

2.1. Sample's fabrication

DCB specimens (290 mm long, 25 mm wide, and 12.5 mm thick) were fabricated using high-strength steel DIN 40CrMoMn7, whose mechanical properties can be found in [57]. Before bonding, adherents were sandblasted and then cleaned using acetone. The structural 3M Scotch-Weld™ 9323 B/A adhesive was manually mixed and applied on the substrates. An adhesive thickness of 0.3 mm was ensured by adding 2% by weight of glass

microspheres with 300 μm of diameter. Finally, a razor blade was used to ensure a sharp notch at the beginning of the bondline.

Specimens were cured in an oven in three steps: a linear temperature ramp from room temperature to 65°C for 1.5 hours, two hours of stable hold at 65°C, and a descending temperature ramp until the room temperature for 2 hours. Table 1 present the specimens' description and the main adhesive's properties. Since for the first set of samples, with 82 mm of the length of starting notch, a smaller region of the bondline was included in the DIC region of interest, this study also considered another set of specimens with a shorter initial crack length equalling 65 mm. In both cases, an initial cohesive failure was introduced.

Table 1: Specimen's description and adhesives' main properties.

Young's modulus [MPa]	**2569 ± 158**	
Ultimate stress [MPa]	38.7 ± 0.2	
Length of starting notch (a_0) [mm]	82	65
Specimen's name	S_82_1 S_82_2	S_65_1 S_65_2
Number of samples	2	2

For the Digital Image Correlation analysis, a fine speckle pattern was painted on the lateral surface of the specimens. First, the lateral surface of the sample was covered with a thin layer of white water-based painting, then an arbitrary aerosol of black paint was applied.

2.2. DCB tests

An MTS electro-mechanical testing machine with a load cell of a maximum capacity of 100 kN was used to perform quasi-static DCB tests. The load cell accuracy is 0.5% since it is calibrated according to ISO 7500-1 [58] (rated class 0.5). Furthermore, a test speed rate of 0.5 mm/min was applied, as recommended by the ISO 25217 [59] standard. In addition, load and the machine's crosshead displacement (δ) were also recorded during the whole test, and their curves are drawn in Figure 1.

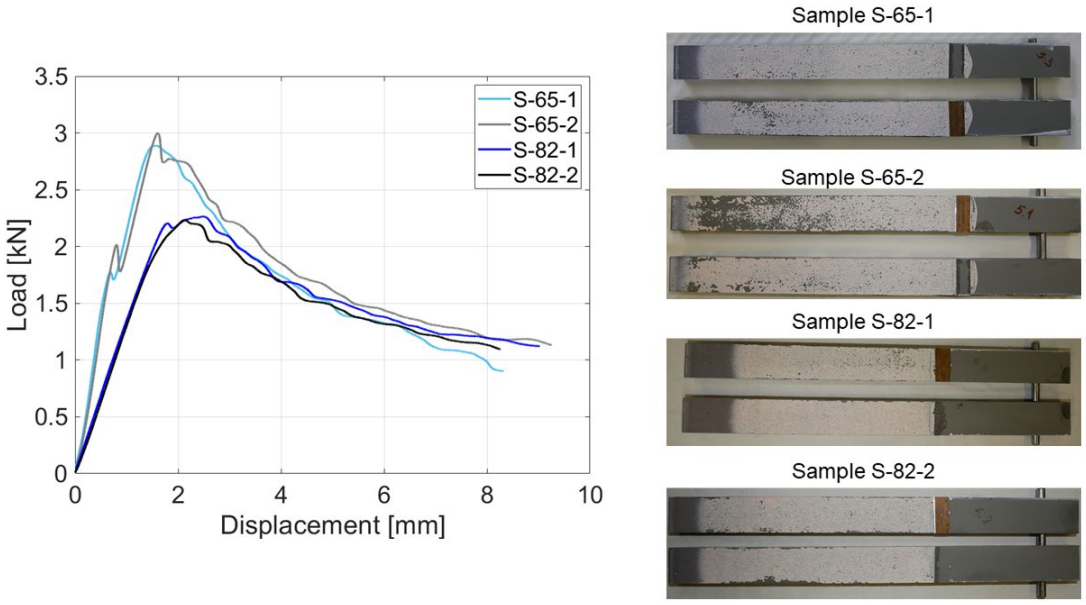

Figure 1: Representative experimental load versus crosshead displacement curves and detail of the fractured surfaces.

As shown in Figure 1, the test is characterised by an increase in the loading until it achieves the maximum value, followed by a crack propagation phase where the load decreases until final failure. Specimens S-65-1 and S-65-2 present a more rigid behaviour since their initial crack length is smaller than S-82-1 and S-82-2. Further discussion about the DCB experimental results is addressed in section 4.

2.2.1. Visual crack length estimation and DIC measurement set-up

The visual crack length estimation was performed using the same acquisition system of the DIC (GOM – 3D Aramis adjustable system), using a 2 Hz acquisition frequency. The DIC measurement system includes two adjustable cameras with 12 Megapixels of resolution, dual-LED lights (10°), Titanar B 75 mm lens type with an aperture of 22 mm, and stereo-angle equals to 25°. The chosen hardware system presents a field of view equal to 110 mm and an image scale of 39 pixels/mm.

Before the tests, the DIC system was calibrated using a CP 40/MV panel set at one specific stand-off distance of 697 mm (recommended for the selected measuring volume – 100 x 80 x 80 mm^3) to adjust the temperature and image distortions. After that, a calibration deviation of around 0.04 pixels was found.

The DIC acquisition system could synchronise each frame with the corresponding load and displacement values recovered from the testing machine. The post-processing software used was the GOM correlate (version 2018), a subset size of 33 pixel and step sizes of 11 pixels were defined.

2.2.2. Acoustic emission acquisition set-up

During quasi-static DCB tests, the complete AE measurement chain was composed of two Vallen VS150-M piezoelectric resonant transducers (resonant working frequency in the range 100-450 kHz), each equipped with a 34 dB Vallen AEP5 preamplifier and connected to an eight-channel Vallen ASMY-6 acquisition unit through low-noise cables. Moreover, the rules for acquiring AE events and managing the obtained data were defined using Vallen AE-Suite Software R2017.0504.1.

The OKS-1110 silicone grease was used to couple the sensors on the samples and ensure continuity during AE signals transmission between the specimen surface and sensors. In

addition, magnetic holders were also applied to maintain the sensors in a fixed position during the whole test (Figure 2a).

Table 2 shows the main AE acquisition parameters used during DCB tests, calibrated based on the pencil-lead break (PLB) test (ASTM E976 [60]). This test [61], also called Hsu-Nielsen test, produced artificial AE sources by breaking a pencil lead (hardness of 2H and diameter of 0.3 mm) at an angle of 30° on the sample's surface. As a result, it was possible to analyse the signal attenuation related to the distance of the sensors and determine their optimal position, as shown in Figure 2b. Finally, it is worth adding the parametric features of the AE transient hits (i.e., amplitude, counts, duration, energy, and rise-time) and their full waveforms were recorded during the tests adopting the sampling rates reported in Table 2.

Table 2: Acoustic emission acquisition parameters.

Sampling rate for the acquisition of AE features	10 MHz
Sampling rate for the acquisition of AE transient waveforms	5 MHz
Amplitude threshold (with respect to a reference voltage amplitude of 1 µV)	34 dB
Rearm time	2.5 ms
Cut-off-frequency (minimum frequency of acquisition)	25 kHz
Pre-trigger	750 samples
Post-trigger	750 samples
Duration discrimination time (time window to register each AE signal)	400 µs

Fundamental antisymmetric wave (A0) velocity	3181 m/s
Digital pass-band filter	25kHz-250kHz

It is worth mentioning that a correct amplitude threshold value is a crucial parameter for AE acquisition since it represents the minimum value considered to have the AE events recorded. Therefore, a first acquisition was made, without performing the mechanical test so to identify the amplitude values of AE events just related to the environmental noise, in order to well-define this parameter. As a result, the threshold value of 34 dB was set.

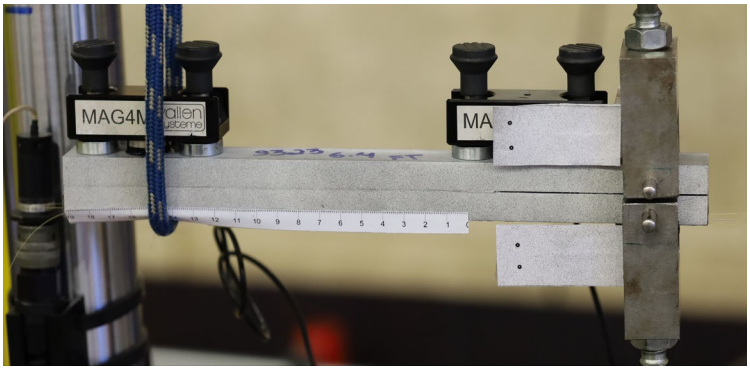

(a)

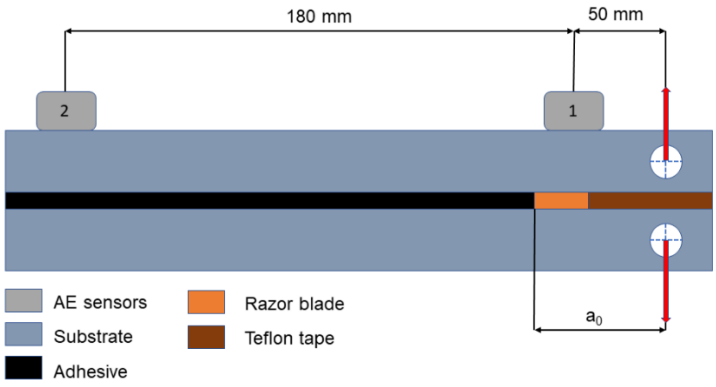

(b)

Figure 2: (a) Acoustic emission sensors positioned during the DCB tests and (b) scheme showing the main distances used to position the sensors.

The velocity value, adopted for the research and reported in Table 2, was determined considering the sound velocities of symmetric (S0 and S1) and antisymmetric (A0 and A1) wave modes, propagating in 12.5 mm thick plates made of the adopted steel grade, and their dispersion curves (Figure 3) experimentally derived by a dedicated PLB test. The Vallen acquisition system (AMSY-6) and the Vallen Control Panel software (v. R2017.0504.1) were used on purpose.

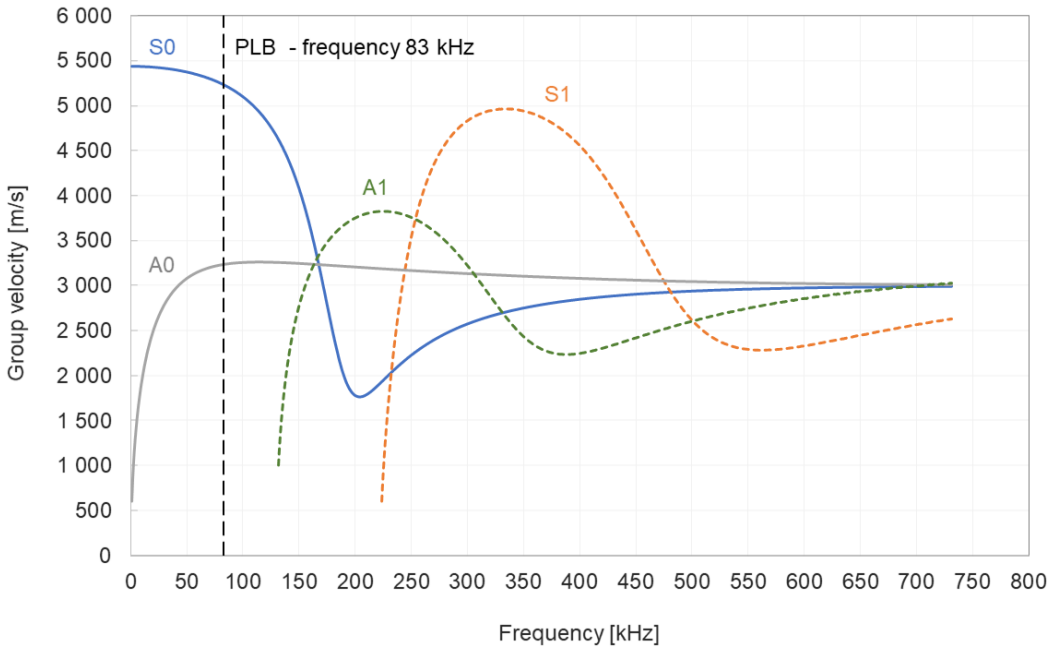

Figure 3: Dispersion curves of high-strength steel DIN 40CrMoMn7 plates - thickness of 12.5 mm.

The PLB test was performed once the distance between the sensors was defined (as shown in Figure 2b). Since the highest peak frequency of AE events acquired during the PLB test was found to be equal to 83 kHz and just the fundamental symmetric (S0) and antisymmetric (A0) wave modes seem to be present in this region of the dispersion diagram, the velocity of both fundamental wave modes was used to localise the PLB sources and perform a comparison of the localization performance.

To the aim, the Vallen system was applied again through its localisation tool. Such a tool simply acquires the times-of-arrival to each sensor of the same AE source and, then, triangulates and determines its position considering the distance between the sensors and the velocity group of the considered wave. The velocity providing the lowest localization error resulted to be the fundamental antisymmetric (A0) one.

It is also worth anticipating here a feature of the AE events acquired during DCB tests: the peak frequency of the events characterized by the highest amplitudes seems to lie between 90 and 150 kHz (Figure 4) and the A0 group velocity seems to be significantly less dispersive in this frequency range (Figure 3) with respect to the symmetric (S0) mode.

Based on the reported observations, the velocity of the antisymmetric wave mode (A0), equal to 3181 m/s (Table 2), was adopted in the following of the research.

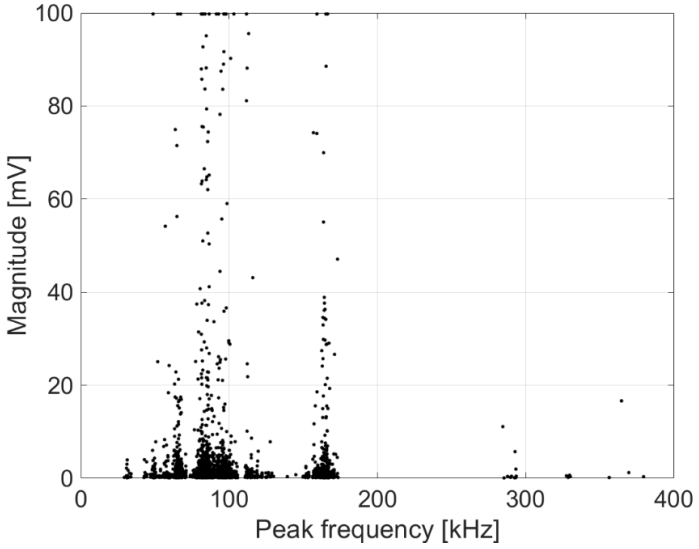

Figure 4: Peak frequency of the localised events in the function of their magnitude – sample S-81-1.

3. POST-PROCESSING OF ACOUSTIC EMISSION RAW DATA

After each DCB test, AE raw data were analysed and post-processed. For the sake of clarity and simplicity, this Section is built considering the exemplificative case of specimen S-82-1. The other specimens were treated in the same way and showed analogous results.

Figure 5 shows an example of the AE signal's amplitude responses during the mode I fracture propagation test assessed by sensors (channels) 1 and 2; specifically, about 26000 waveforms were recorded from the test on specimen S-82-1.

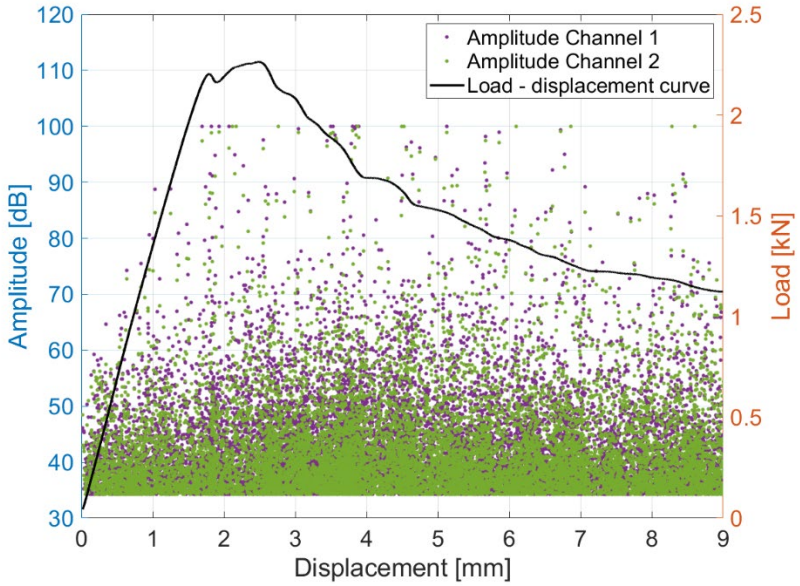

Figure 5: Amplitude values of acoustic emission raw data during DCB test of sample S-82-1.

The AE acquisition system is sensitive to background noise, so the massive number of recorded waveforms probably does not represent just AE events associated to adhesive's fracture mechanisms [35], [39], [62]. Therefore, looking at Figure 5, it is not possible to draw any further conclusion about the AE waveforms and the crack propagation within the bondline. So, to have an accurate AE analysis, it was crucial to implement a well-defined post-processing procedure, which will be described in the following sections.

3.1. Classification and clustering of acoustic emission events

An unsupervised artificial neural network was chosen for the post-processing procedure since previous information about the AE events outputs was unknown before the tests. Therefore, it was necessary to identify the main significative waveform parameters and their better correlation from the input data.

The main features of AE waveforms are peak frequency, amplitude, energy, counts (number of times the AE waveform crosses the threshold level), duration, and rise-time [10], [26], [35], [63]. A parallel coordinates plot was built to identify the best correlation between the waveform features for pattern recognition and high-dimensional data classification, Figure 6. To improve data visualisation, comparison between different features and comprehension, each of the axes of such a plot runs from 0 to 1. Each piecewise line running from one axis to the adjacent ones represents the set of relevant features for a given AE event. In order to be correctly plotted, the features must be first normalized to match the 0-to-1 range of the axes and, to improve the effectiveness of the plot, subdivided into four groups equally ranged on a 0.25 span based on a reference feature (the duration, in the present case). In this way, the intersection of the piecewise lines with the vertical axes shows the distribution of the relevant features and their possible relationships and correlations.

The duration and energy features present a fair correlation because, generally, the 0.25 span lines do not cross each other running form the duration axis to the energy one, but, on the other hand, the two features show a different distribution along the respective axes. Then, both features were chosen as input values to be applied on the Self-Organising Map (SOM) algorithm. This algorithm generates a 2D topological map that classifies the input data regarding their similarities by using a neighbourhood function (Euclidean distance), as detailed in [4], [39], [25].

The last plot of Figure 6 shows the SOM outputs of the analysed data, considering the duration and energy as input values. These hexagonal lattice maps represent similar input values in proximity and dissimilar ones far away, classifying the AE data based on the

input's relative distances. However, it is not possible to divide the data into classes/clusters at this step. For that, an additional K-means iterative algorithm was implemented, as well. The optimal number of clusters instead was determined by evaluating the performance of different indexing criteria (Davies-Bouldin, Silhouette, and Calinski-Harabasz), as described in [39], [42].

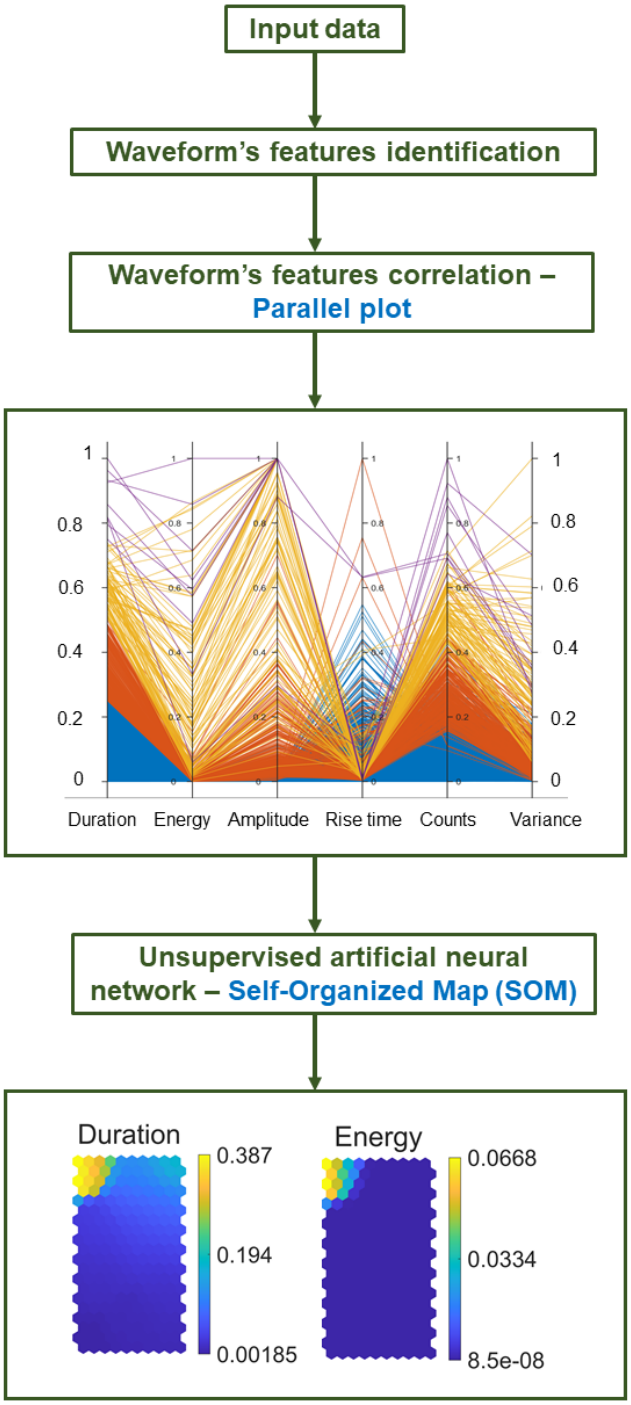

Figure 6: Pattern recognition and classification procedure adopted in the AE analysis – sample S-82-1.

The performance evaluation of the indexing criteria determined an optimal number of clusters equal to three. After that, the K-means algorithm was applied, and three different clusters were created, considering the lowest root-mean-square error between the distance of the centroid and the input values of each dataset group. Figure 7 shows the energy [eu – "energy unit" equals 10^{-18} J] versus duration graph of the sample S-82-1 clustered results and some examples of the waveforms from each group.

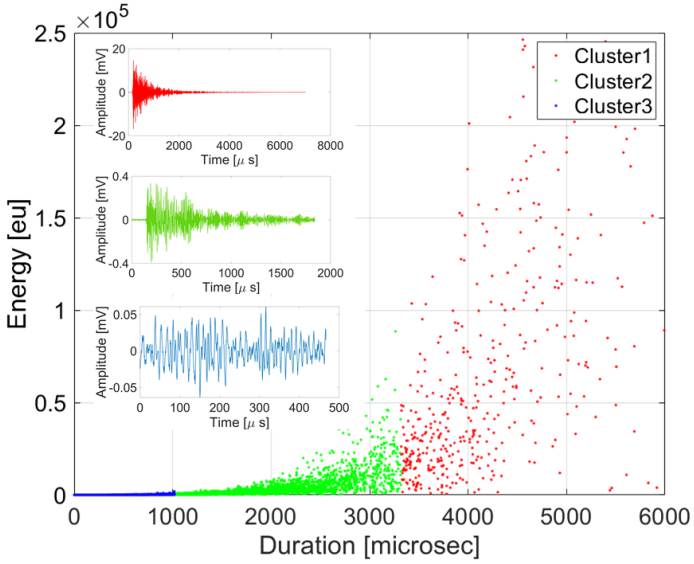

Figure 7: Clustering results based on the energy and duration features with representative waveforms of each cluster – sample S-82-1.

Cluster one of sample S-82-1 contains about 2.5% (646 hits), cluster two includes 16.2% (4228 hits), and cluster three 81.3% (21289 hits) of the total waveforms. To draw further conclusions about the physical meaning of each cluster, their waveform's morphology was analysed. As can be seen in Figure 7, cluster one, represented by a red waveform, is a burst (the type of hit that often is associated with damage development in a material), cluster two typical waveform (green colour) also presents a morphology similar to a burst, but with high levels of noise. Finally, the blue waveform shows the morphology of a continuous wave, generally related to background noise. It is also worth noticing that the amplitude maximum level decreases of one order of magnitude switching from cluster one to cluster

two and of another order of magnitude switching from cluster two to cluster three. This is typically observed switching from emissions due to damage to those related to background noise.

Nevertheless, just looking at the hits' morphology, it is not sufficient to choose the clusters to be analysed. So, the cumulative energy was used as an additional feature to identify the clusters related to the damaging mechanisms inside the adhesive joints. This feature sums the energy introduced in the system by each hit during the whole acquisition time, and its trend is shown in Figure 8.

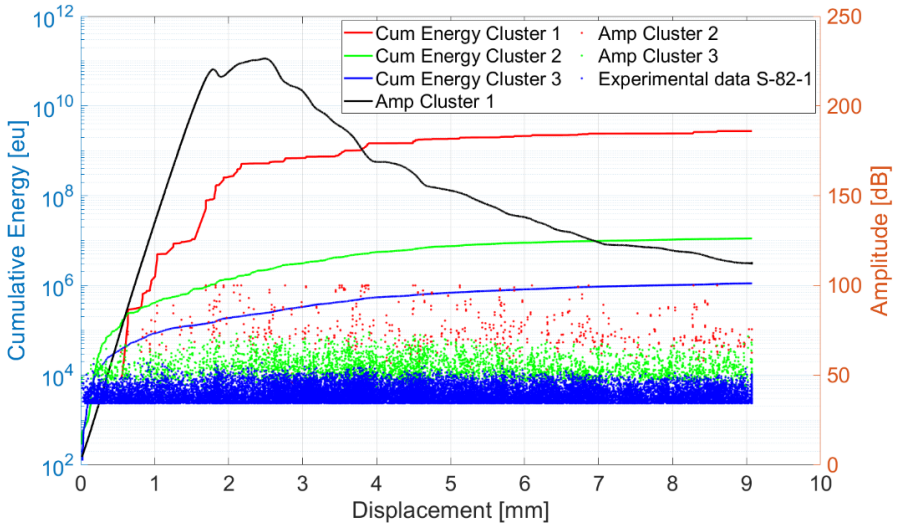

Figure 8: Acoustic emission clustering results – cumulative energy of each cluster of data – sample S-82-1.

As shown in Figure 8, the three different clusters present different levels of cumulative energy with a significant difference in their orders of magnitude. Knowing that damage propagation often produces hits with high energy levels and background noises typically have AE waves with lower and constant energy levels, the two clusters with relevant cumulative energy levels (1 and 2) were chosen for further analysis.

It is worth mentioning that the specimens did not present large dimensions so, the sensors can also record reflections of major AE hits. Considering that after each reflection, the energetic level of an AE signal gets lower, the amount of reflected AE hits inside the highest energetic clusters should be lower.

The AE events of sample S-82-1 before (26163 hits) and after (4874 hits) the clustering procedure represent a reduction of around 80% on the total amount of hits. However, as shown in Figure 6, the highest amplitude values were maintained, indicating that the most relevant hits were still included in the analysed groups.

It was also observed that the first jump in the amplitude values (red dots) happened around 1 mm of the test crosshead displacement, indicating crack initiation. Then, at the maximum load, a significant jump on the cumulative energy of cluster one is observed, marking the beginning of crack propagation.

3.2. Localisation of acoustic emission events

Once the clusters associated with damage mechanisms were defined, it was possible to estimate AE source's localisation. A 1D algorithm based on the distance between the sensors, wave velocity, and AE hits' time-of-arrival was used.

The distance between the sensors was the same for all the specimens and equal to 180 mm.

Before the time-of-arrival picker calculation, the AE signals were arranged in events. Each event should contain at least two different sensor hits that were used for the source's localisation. To establish that two AE signals belong to the same event, their onset times difference must not exceed 0.5 μs. This value was obtained by dividing the distance between the sensors by the wave velocity.

Finally, three different types of ToA picker algorithms were considered and applied to estimate each hits' time-of-arrival: the Akaike Information Criteria (AIC) picker, Threshold Adopted to Maximum Amplitude Signal (TAMAS), and Baer and Kradolfer pickers [54], [55].

The automatic time-of-arrival calculation by the AIC picker is based on the difference in onset times between the two signals belonging to the same AE event. First, the AE waveforms were transformed using the Hilbert transformation, considering a wave's time window two times equals the pre-trigger duration. After that, the AIC function is calculated [55], [64], [65]. Finally, the minimum of the AIC function determines the onset time of the analysed hit, as detailed in Figure 9.

The TAMAS is a simple picker based on determining the source's time-of-arrival by identifying the instant when the signal crosses a fixed threshold. The threshold is calculated as a percentage of the maximum amplitude of each signal. This percentage represents the signal-to-noise ratio, and for the studied samples, the best value found is equal to 1%, determined by a manual trial and error calculation.

The Baer and Kradolfer picker is an automatic phase picker based on modifying Allen's envelope function by squaring it and adding its variance to determine a specific AE wave's characteristic function [54]. This Characteristic Function (CF) is used to identify and quantify changes in the wave's morphology, sensitive to amplitude, frequency, and phase changes. Once the CF is determined, it is integrated into a dynamic threshold to identify when the CF exceeds the set threshold [66], [67]. Also, for this picker algorithm, a wave's time window two times equal to the pre-trigger duration was used.

Once the different algorithms defined the time-of-arrival, it was possible to calculate the AE source's localisation using Equation 1:

$$l_1 = \frac{1}{2}(l_t - \Delta t * V) \qquad \text{Equation (1)}$$

where l_1 represents the AE source's distance from the first sensor, l_t the total distance between the sensors, Δt the difference between the hits identified in each event and V the wave velocity. After calculating the AE source's distance from sensor one, the crack length was determined by summing the measured length between the centre position of sensor one and the sample's loading point (50 mm).

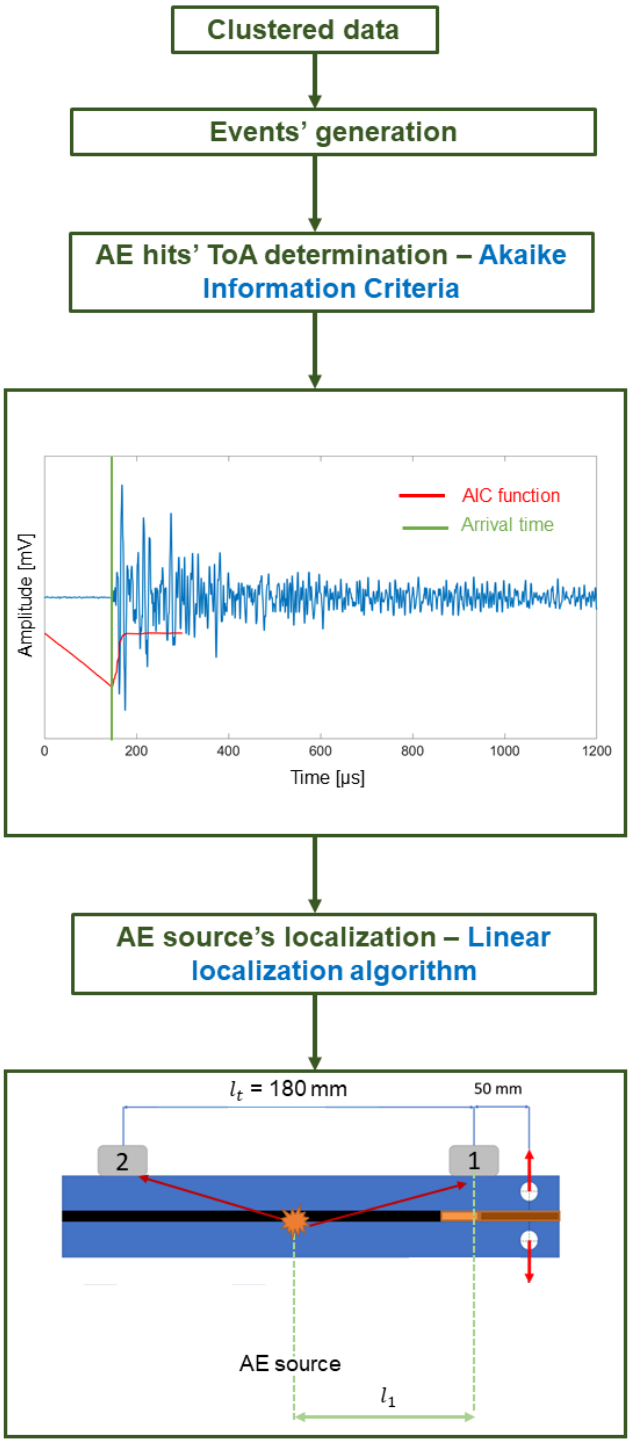

Figure 9: Localisation procedure, from the clustered data, for the determination of AE source's position (exemplificative case of AIC time-picker algorithm).

A Hsu-Nielsen test was systematically applied to select the most accurate time-picking algorithm for the final AE source's localisation. For that, the pencil lead was broken in some known positions. Finally, the time-picker and 1D localisation algorithms were used to determine the AE source's position. The localisation results and the Root Mean Squared Error (RMSE) are shown in Figure 10 and Table 3.

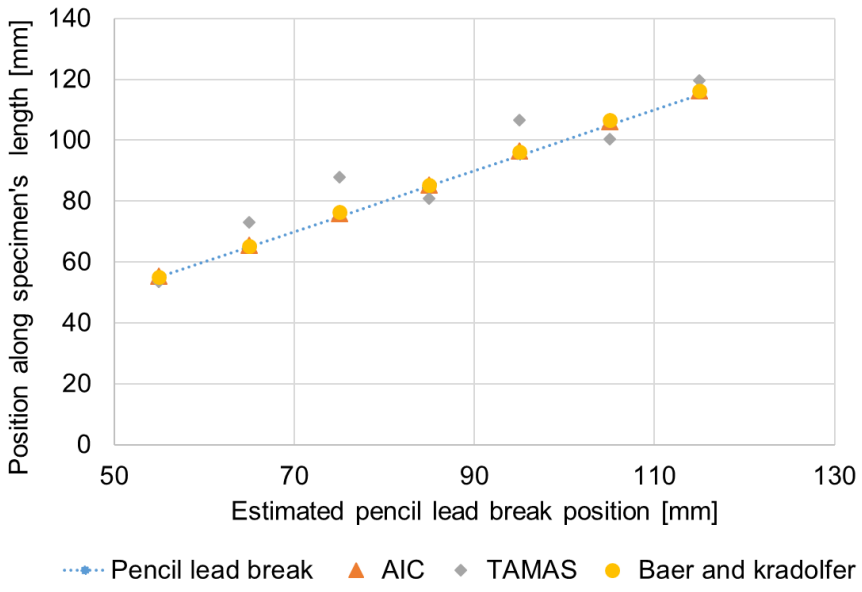

Figure 10: Comparison between time-of-arrival pickers.

Table 3: Comparison of localisation results using different pickers – sample S-82-1.

Time-picking algorithms	AIC	TAMAS	Baer and Kradolfer
RMSE	**0.91**	**9.01**	**1.02**

The localisation results using the AIC and Baer and Kradolfer pickers presented the lower RMSE indicating a higher accuracy of the predicted results by the squared regression when compared with the actual AE responses produced by the artificial sources, which means that the AE localised hits are more concentrated in the neighbourhood of the best fit. Therefore, the AIC picker was chosen to be applied for further analysis since it is also a user-independent method and requires less computational time to estimate the AE source's location when compared with the Baer and Kradolfer algorithm.

4. RESULTS AND DISCUSSION

In this Section, crack length estimation by visual evaluation and DIC is described. Then, AE localisation results are discussed and compared to visual and DIC ones.

4.1. Crack length estimation by visual evaluation and DIC

Crack length estimation by visual evaluation and DIC methods was done using the GOM correlate software. For both methods, around forty frames were analysed, from the maximum load until the maximum opening that can be assessed within the measurement volume of the DIC system.

The visual evaluation was based on the visual identification of the crack-tip, based on the determination of two main points for each frame: the razor blade's tip and the crack-tip's position of each analysed frame. Once these two points were identified, the total crack length was estimated by adding the crack-tip point position with the razor blade position using the software's distance measurement tool [22]. It is worth mentioning that a ruler was also attached to the specimen for measurement cross-checking.

Using virtual extensometers, DIC was applied to measure the sample's opening displacement in each analysed frame [68], [69]. From each analysed opening displacement curve, it was possible to identify two different zones, a constant and a variable one, as

shown in Figure 11. The point representing the transition between both displacement zones is called the “DIC opening point”.

To understand the physical meaning of the DIC opening point in the fracture mechanisms of the DCB specimen, the corresponding strain (in the y-direction) of the bondline was calculated by dividing the sample’s relative vertical displacement by the adhesive’s thickness. Only the bondline strain was considered since young’s modulus of the substrates is considerably higher than the adhesive’s one, as described in [22]. Thus, a strain of around 1.4% was calculated in the position of the DIC opening point.

Comparing this value with the adhesives’ bulk tensile test, it was noticed that at about 1% of strain, the adhesive 9323 changes its mechanical behaviour, and its plasticisation starts, as shown in Figure 10. This suggests that the DIC opening point for this adhesive represents the onset of plasticisation in the adhesive [22].

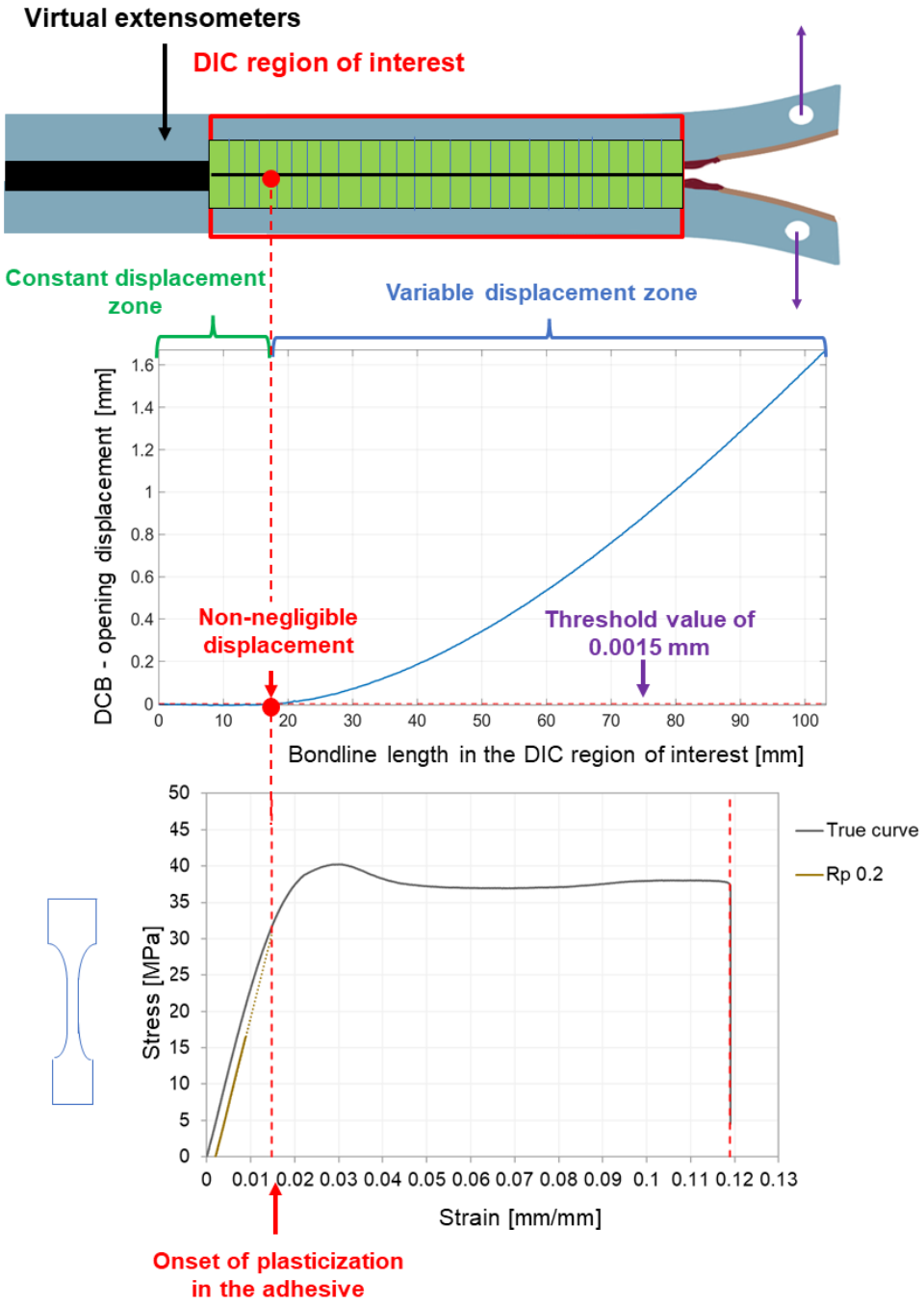

Figure 11: Scheme of DIC opening point determination and association of the adhesively bondline strain calculated in the position of the DIC opening point with the beginning of plasticisation in the adhesive, obtained by a bulk tensile test.

Figure 12 shows the comparison between the DIC opening points and the visual evaluations vs. the applied load. The right vertical axis, x [mm], corresponds to the horizontal position along the specimen, starting from the loading point.

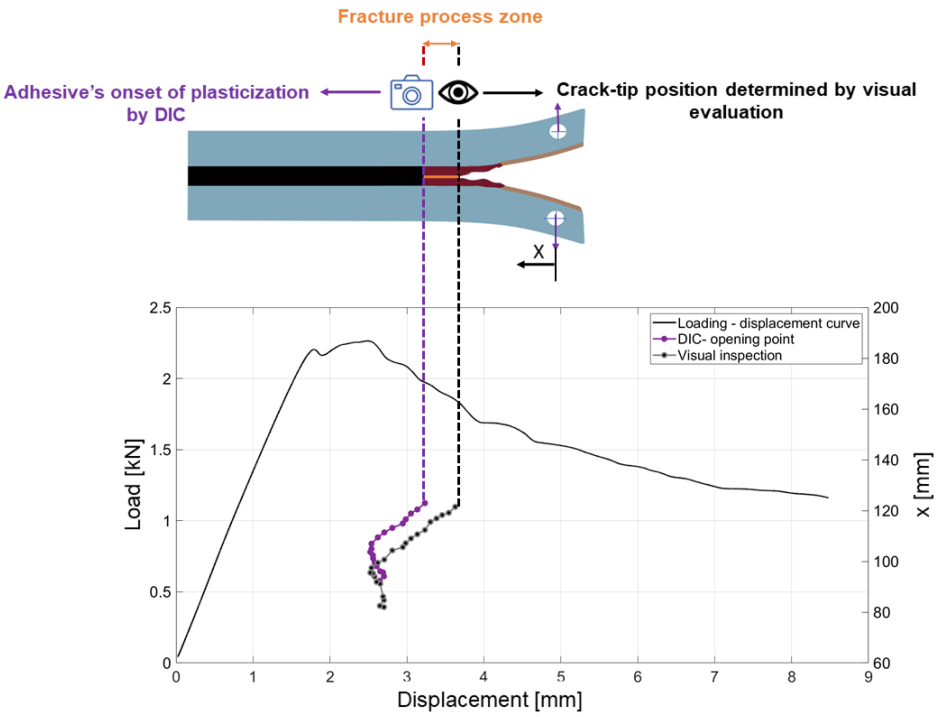

Figure 12: Visual evaluation and DIC opening point positions along the sample's length during the DCB test – sample S-82-1.

As shown in Figure 11, the DIC opening points and visual evaluation values did not have the same position. Knowing that the visual evaluation points identified the position of the already fractured adhesive and the DIC opening point represents the position of the onset of plasticisation of the adhesive, the distance between them can be associated with the length of the Fracture Process Zone (FPZ) [20][68]. A maximum FPZ length of around 12 mm was evaluated.

4.2. Acoustic emission localisation results and comparison with other techniques

Figure 13 showcases, on the horizontal axis, the values of the load recorded during the test and, on the vertical axis, the position along the x axis of the AE localisation results and the position of the opening point detected by DIC. All the performed tests are reported.

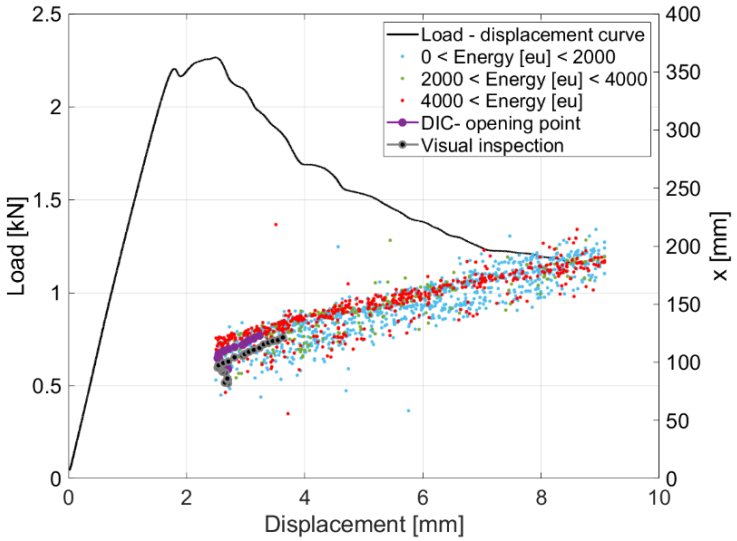
Load - displacement curve
0 < Energy [eu] < 2000
2000 < Energy [eu] < 4000
4000 < Energy [eu]
DIC- opening point
Visual inspection
Load [kN]
x [mm]
Displacement [mm]

(a)

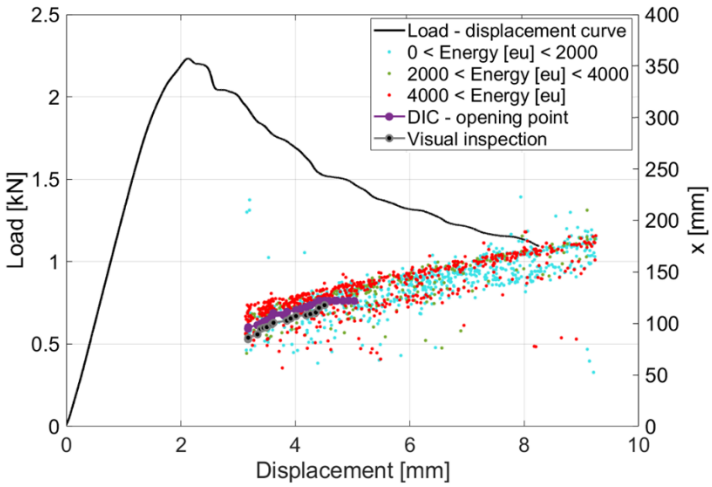
Load - displacement curve
0 < Energy [eu] < 2000
2000 < Energy [eu] < 4000
4000 < Energy [eu]
DIC - opening point
Visual inspection
Load [kN]
x [mm]
Displacement [mm]

(b)

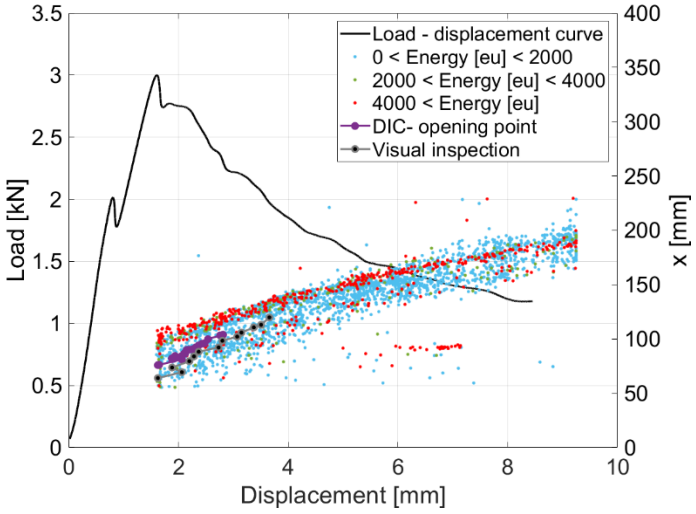
Load - displacement curve
0 < Energy [eu] < 2000
2000 < Energy [eu] < 4000
4000 < Energy [eu]
DIC- opening point
Visual inspection
Load [kN]
x [mm]
Displacement [mm]

(c)

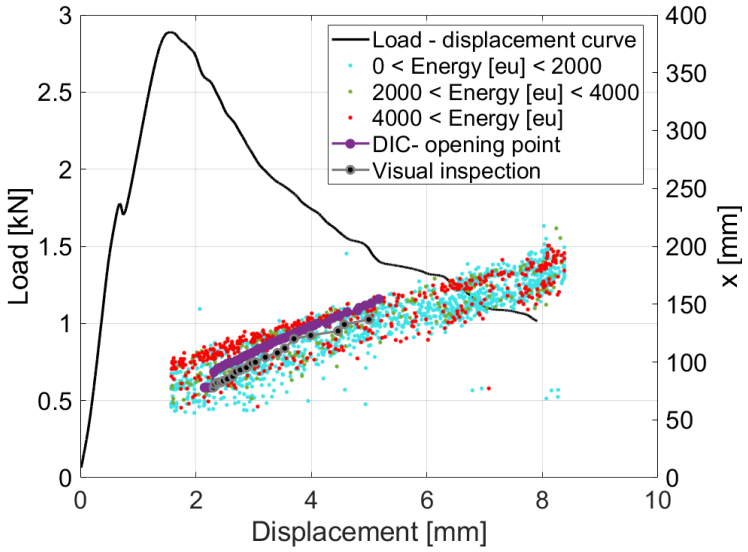

(d)

Figure 13: Acoustic emission localisation results compared with the visual evaluation and DIC measurements (a) S-82-1, (b) S-82-2, (c) S-65-1 and (d) S-65-2.

The DIC opening point and visual evaluation curves are shorter than the AE localised data due to limitations in the region of interest of the DIC acquisition system, which permits a maximum measurement length of 110 mm. AE results resulted to be scattered, but still followed the crack propagation trend observed by the DIC and visual evaluation methods.

As shown in Figure 13, an additional analysis was done by subdividing the AE localised hits with respect to their energy values, to obtain further information about the damage mechanisms within the adhesively bonded joints.

All specimens present a well-defined high energetic group represented by the red dots (energy higher than 4000 [eu]), with the AE source's position quite ahead of the crack-tip (determined by a visual evaluation). It is worth mentioning that the value of 4000 [eu] was chosen because it is the lowest energy level at which a clear distinction of localised AE signals could be observed. Since the studied adhesive is ductile and, consequently, it has an non negligible process zone, a fracture mechanism ruled by plastic deformations before the crack-tip that increases the amount of absorbed energy during the crack propagation

process is expected [70]. Moreover, as already known in the literature, AE hits generated by plastic deformation and crack initiation are more energetic than those produced by crack propagation [35].

The higher energetic group also showed a similar trend as the DIC opening point values, indicating that these AE hits can also be associated with the onset of plasticisation within the adhesive. Instead, the low energetic groups could be related to friction and crack propagation inside the adhesive joint [47]. All specimens presented (Fig. 13) similar results independently of the crack initial length.

More insight on the damage mechanisms that occurred within the bondline could be gained by considering cavitation.

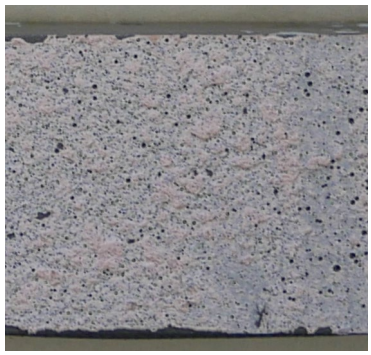

Figure 14: Detailed fracture surface of the S-82-1 tested specimen.

Figure 14 showcases the fracture surface of S-82-1 specimen. In this and in all the other specimens, the adhesive presented dimples on its surfaces, indicating that the specimens are likely to have undergone cavitation phenomena due to the triaxial stresses produced during mode I fracture tests, as described by K. Kamiyama *et al*. [71]. This phenomenon can occur ahead of the crack-tip, mainly in ductile adhesives, increasing the adhesive's plastic deformation and the joint's fracture energy, as stated by Lee et al. [72].

So, the high energy level group identified on the samples maybe can be associated with AE hits produced during the generation of voids during the cavitation within the adhesive, and

the remaining AE events could instead be related to other failure mechanisms, such as coalescence of micro-voids, brittle fracture parts (flatter zones), and adhesive cracking [73]. New experiments specifically designed to correlate AE events to cavitation are needed to confirm this hypothesis.

Finally, the AE method using the studied ANN post-processing method showed to be an efficient method to localise damage within adhesive joints under pure mode I. From the analysis of AE amplitude, it was possible to identify two main steps: damage initiation followed by crack propagation. In addition, the AIC function presented effective results for the AE source's time-of-arrival determination, being a recommended method to be applied in this type of analysis.

For the studied adhesive, the results suggest that the AE method could identify the already fractured adhesive and the onset of plasticisation of the adhesive (DIC opening point position) ahead of the crack-tip, opening new perspectives for its application as a monitoring system of adhesively bonded joints.

The feasibility of the AE monitoring system of adhesive joints under fatigue loading will be investigated in future work. In fatigue loading, different failure mechanisms and a smaller process zone are expected, so it is necessary to investigate if the acoustic emission method still identifies the crack propagation trend of the adhesives and if the subdivision of the AE events in different energy levels can provide further information to identify the fracture mechanisms of the specimens.

5. CONCLUDING REMARKS

The feasibility of using the AE method to size the crack length and monitor crack growth in adhesively bonded DCB specimens was investigated. The AE responses were clustered and analysed based on a non-supervised artificial neural network algorithm. The main results were compared with DIC and visual inspection. As a result, the main conclusions can be stated:

- the DIC opening point represents the onset of plasticisation in the adhesive, as discussed in [20]. Therefore, the distance between the DIC opening point and the crack tip observed by visual inspection can be interpreted as the length of the fracture process zone;
- AE results could correctly follow the trend of crack propagation during the test. However, the AE responses are highly scattered with respect to other methods such as DIC and visual inspection;
- the further classification of the AE hits regarding their energy levels showed that the high-energetic level group presents a similar trend with the DIC measurements, suggesting that for the considered adhesive, the AE method could identify the onset of plasticisation of the adhesive. It is a relevant feature for applying the AE as an in-service monitoring method, indicating that the damage in ductile adhesives can be identified before failure;
- AE is a promising method for damage monitoring in adhesively bonded joints since it can be applied in in-service conditions and not just in a laboratory, contrarily to other effective methods characterised by heavy and bulky equipment.

6. ACKNOWLEDGEMENT

Support by the Italian Ministry for Education, University, and Research through the project Department of Excellence LIS4.0 (Integrated Laboratory for Lightweight e Smart Structures) is acknowledged. PoliNDT (Interdepartmental Lab for NDT and SHM set at Politecnico di Milano) is also acknowledged for providing the AE equipment.

REFERENCES

[1] M. D. Banea, L. F. M. Da Silva, R. D. S. G. Campilho, and C. Sato, “Smart adhesive joints: An overview of recent developments,” *J. Adhes.*, vol. 90, no. 1, pp. 16–40, 2014.

[2] M. D. Banea, M. Rosioara, R. J. C. Carbas, and L. F. M. da Silva, “Multi-material adhesive joints for automotive industry,” *Compos. Part B Eng.*, vol. 151, no. May, pp. 71–77, 2018.

[3] M. D. Banea and L. F. M. Da Silva, “Adhesively bonded joints in composite materials: An overview,” *Proc. Inst. Mech. Eng. Part L J. Mater. Des. Appl.*, vol. 223, no. 1, pp. 1–18, 2009.

[4] A. Refahi Oskouei, H. Heidary, M. Ahmadi, and M. Farajpur, “Unsupervised acoustic emission data clustering for the analysis of damage mechanisms in glass/polyester composites,” *Mater. Des.*, vol. 37, pp. 416–422, 2012.

[5] S. Masmoudi, A. El Mahi, S. Turki, and R. El Guerjouma, “Mechanical behavior and health monitoring by Acoustic Emission of unidirectional and cross-ply laminates integrated by piezoelectric implant,” *Appl. Acoust.*, vol. 86, pp. 118–125, 2014.

[6] O. Sam-Daliri, L. M. Faller, M. Farahani, and H. Zangl, “Structural health monitoring of adhesive joints under pure mode I loading using the electrical impedance measurement,” *Eng. Fract. Mech.*, vol. 245, no. February, p. 107585, 2021.

[7] A. Vargalui, M. Martinez, D. S. Zarouchas, and S. Pant, “Temperature effects on an acoustic emission based SHM system - Applied to composite materials,” *26th Int. Conf. Adapt. Struct. Technol. ICAST 2015*, no. October, 2015.

[8] Y. WANG, C. GOGU, N. BINAUD, C. BES, R. T. HAFTKA, and N. H. KIM, “A cost driven predictive maintenance policy for structural airframe maintenance,” *Chinese J. Aeronaut.*, vol. 30, no. 3, pp. 1242–1257, 2017.

[9] P. Manco, M. Caterino, R. Macchiaroli, M. Rinaldi, and M. Fera, “Aircraft Maintenance: Structural Health Monitoring Influence on Costs and Practices,” *Macromol. Symp.*, vol. 396, no. 1, 2021.

[10] M. Carboni and A. Gianneo, “Feasibility of an acoustic emission based structural health monitoring for railway axle under fretting fatigue damage,” *14th Int. Conf. Slov. Soc. Non-Destructive Test. "Application Contemp. Non-*

Destructive Test. Eng. Conf. Proc., vol. 2017-Septe, pp. 65–72, 2017.

[11] C. Kralovec and M. Schagerl, "Review of structural health monitoring methods regarding a multi-sensor approach for damage assessment of metal and composite structures," *Sensors (Switzerland)*, vol. 20, no. 3, pp. 1–25, 2020.

[12] M. Mitra and S. Gopalakrishnan, "Guided wave based structural health monitoring: A review," *Smart Mater. Struct.*, vol. 25, no. 5, 2016.

[13] K. Wang, M. Liu, W. Cao, W. Yang, Z. Su, and F. Cui, "Detection and sizing of disbond in multilayer bonded structure using modally selective guided wave," *Struct. Heal. Monit.*, pp. 1–13, 2019.

[14] Z. Su, L. Ye, and Y. Lu, "Guided Lamb waves for identification of damage in composite structures: A review," *J. Sound Vib.*, vol. 295, no. 3–5, pp. 753–780, 2006.

[15] B. Ren and C. J. Lissenden, "Modal content-based damage indicators for disbonds in adhesively bonded composite structures," *Struct. Heal. Monit.*, vol. 15, no. 5, pp. 491–504, 2016.

[16] E. P. Carden and P. Fanning, "Vibration based condition monitoring: A review," *Struct. Heal. Monit.*, vol. 3, no. 4, pp. 355–377, 2004.

[17] M. Z. Sadeghi *et al.*, "Damage detection in adhesively bonded single lap joints by using backface strain: Proposing a new position for backface strain gauges," *Int. J. Adhes. Adhes.*, vol. 97, no. November, 2020.

[18] J. H. L. Grave, M. L. Håheim, and A. T. Echtermeyer, "Measuring changing strain fields in composites with Distributed Fiber-Optic Sensing using the optical backscatter reflectometer," *Compos. Part B Eng.*, vol. 74, pp. 138–146, 2015.

[19] M. Kharshiduzzaman, A. Gianneo, and A. Bernasconi, "Experimental analysis of the response of fiber Bragg grating sensors under non-uniform strain field in a twill woven composite," *J. Compos. Mater.*, vol. 53, no. 7, pp. 893–908, 2019.

[20] J. Weiland, M. Z. Sadeghi, J. V. Thomalla, A. Schiebahn, K. U. Schroeder, and U. Reisgen, "Analysis of back-face strain measurement for adhesively bonded single

lap joints using strain gauge, Digital Image Correlation and finite element method," *Int. J. Adhes. Adhes.*, vol. 97, no. November, 2020.

[21] H. Murayama, K. Kageyama, K. Uzawa, K. Ohara, and H. Igawa, "Strain monitoring of a single-lap joint with embedded fiber-optic distributed sensors," *Struct. Heal. Monit.*, vol. 11, no. 3, pp. 325–344, 2012.

[22] R. A. A. Lima, R. Perrone, M. Carboni, and A. Bernasconi, "Experimental analysis of mode I crack propagation in adhesively bonded joints by optical backscatter reflectometry and comparison with digital image correlation," *Theor. Appl. Fract. Mech.*, p. 103117, Oct. 2021.

[23] R. Dugnani, Y. Zhuang, F. Kopsaftopoulos, and F. K. Chang, "Adhesive bond-line degradation detection via a cross-correlation electromechanical impedance–based approach," *Struct. Heal. Monit.*, vol. 15, no. 6, pp. 650–667, 2016.

[24] G. Galanopoulos, D. Milanoski, A. Broer, D. Zarouchas, and T. Loutas, "Health Monitoring of Aerospace Structures Utilizing Novel Health Indicators Extracted from Complex Strain and Acoustic Emission Data," *Sensors*, vol. 21, no. 17, p. 5701, 2021.

[25] M. Saeedifar, M. A. Najafabadi, D. Zarouchas, H. H. Toudeshky, and M. Jalalvand, "Clustering of interlaminar and intralaminar damages in laminated composites under indentation loading using Acoustic Emission," *Compos. Part B Eng.*, vol. 144, no. December 2017, pp. 206–219, 2018.

[26] A. J. Brunner, "Correlation between acoustic emission signals and delaminations in carbon fiber-reinforced polymer-matrix composites: A new look at mode I fracture test data," *32nd Eur. Conf. Acoust. Emiss.*, pp. 55–64, 2016.

[27] R. Mohammadi, M. A. Najafabadi, H. Saghafi, M. Saeedifar, and D. Zarouchas, "The effect of mode II fatigue crack growth rate on the fractographic features of CFRP composite laminates: An acoustic emission and scanning electron microscopy analysis," *Eng. Fract. Mech.*, vol. 241, no. November 2020, p. 107408, 2020.

[28] S. Teixeira de Freitas, D. Zarouchas, and J. A. Poulis, "The use of acoustic emission and composite peel tests to detect weak adhesion in composite structures," *J. Adhes.*,

vol. 94, no. 9, pp. 743–766, 2018.

[29] M. G. R. Sause, S. Schmitt, and S. Kalafat, “Failure load prediction for fiber-reinforced composites based on acoustic emission,” *Compos. Sci. Technol.*, vol. 164, no. December 2017, pp. 24–33, 2018.

[30] D. E. Mouzakis and D. G. Dimogianopoulos, “Acoustic emission detection of damage induced by simulated environmental conditioning in carbon fiber reinforced composites,” *Eng. Fract. Mech.*, vol. 210, no. April 2018, pp. 422–428, 2019.

[31] I. J. Baran, M. B. Nowak, J. P. Chłopek, and K. J. Konsztowicz, “Acoustic Emission from Microcrack Initiation in Polymer Matrix Composites in Short Beam Shear Test,” *J. Nondestruct. Eval.*, vol. 37, no. 1, pp. 1–10, 2018.

[32] W. Roundi, A. El Mahi, A. El Gharad, and J. L. Rebiere, “Acoustic emission monitoring of damage progression in Glass/Epoxy composites during static and fatigue tensile tests,” *Appl. Acoust.*, vol. 132, no. December 2017, pp. 124–134, 2018.

[33] V. Carvelli, A. D’Ettorre, and S. V. Lomov, “Acoustic emission and damage mode correlation in textile reinforced PPS composites,” *Compos. Struct.*, vol. 163, pp. 399–409, 2017.

[34] T. Bohmann, M. Schlamp, and I. Ehrlich, “Acoustic emission of material damages in glass fibre-reinforced plastics,” *Compos. Part B Eng.*, vol. 155, no. April, pp. 444–451, 2018.

[35] M. Saeedifar and D. Zarouchas, “Damage characterisation of laminated composites using acoustic emission: A review,” *Compos. Part B Eng.*, vol. 195, no. December 2019, p. 108039, 2020.

[36] A. Cockerill, K. M. Holford, T. Bradshaw, P. Cole, R. Pullin, and A. Clarke, “Use of high frequency analysis of acoustic emission signals to determine rolling element bearing condition,” *J. Phys. Conf. Ser.*, vol. 628, no. 1, 2015.

[37] F. E. Oz, N. Ersoy, and S. V. Lomov, “Do high frequency acoustic emission events always represent fibre failure in CFRP laminates?,” *Compos. Part A Appl. Sci. Manuf.*, vol. 103, pp. 230–235, 2017.

[38] K. Panasiuk, L. Kyzioł, and K. Dudzik, “The use of acoustic emission signal (AE) in mechanical tests,” *Prz. Elektrotechniczny*, vol. 95, no. 11, pp. 8–11, 2019.

[39] D. Crivelli, M. Guagliano, and A. Monici, “Development of an artificial neural network processing technique for the analysis of damage evolution in pultruded composites with acoustic emission,” *Compos. Part B Eng.*, vol. 56, pp. 948–959, 2014.

[40] E. Lainé, J.-C. Grandidier, M. Cruz, A.-L. Gorge, C. Bouvy, and G. Vaes, “Acoustic emission description from a damage and failure scenario of rotomoulded polyolefin sandwich structure subjected to internal pressure for storage applications,” *Mech. Ind.*, vol. 21, no. 1, p. 105, Jan. 2020.

[41] D. Xu, P. F. Liu, Z. P. Chen, J. X. Leng, and L. Jiao, “Achieving robust damage mode identification of adhesive composite joints for wind turbine blade using acoustic emission and machine learning,” *Compos. Struct.*, vol. 236, no. September 2019, 2020.

[42] E. Pomponi and A. Vinogradov, “A real-time approach to acoustic emission clustering,” *Mech. Syst. Signal Process.*, vol. 40, no. 2, pp. 791–804, 2013.

[43] D. Xu, P. F. Liu, J. G. Li, and Z. P. Chen, “Damage mode identification of adhesive composite joints under hygrothermal environment using acoustic emission and machine learning,” *Compos. Struct.*, vol. 211, no. December 2018, pp. 351–363, 2019.

[44] M. G. Droubi, A. Stuart, J. Mowat, C. Noble, A. K. Prathuru, and N. H. Faisal, “Acoustic emission method to study fracture (Mode-I, II) and residual strength characteristics in composite-to-metal and metal-to-metal adhesively bonded joints,” *J. Adhes.*, vol. 94, no. 5, pp. 347–386, 2018.

[45] A. Maleki, M. Saeedifar, M. Ahmadi Najafabadi, and D. Zarouchas, “The fatigue failure study of repaired aluminum plates by composite patches using Acoustic Emission,” *Eng. Fract. Mech.*, vol. 210, no. December, pp. 300–311, 2019.

[46] W. Xu *et al.*, “Debonding monitoring of CFRP T-joint using optical acoustic emission sensor,” *Compos. Struct.*, vol. 273, no. June, 2021.

[47] “2015_Zouh_ Acoustic emission behaviors and damagemechanisms of adhesively bondedsingle-lap composite joints withadhesive defects.pdf.” .

[48] M. Carboni and A. Bernasconi, *Acoustic Emission Based Monitoring of Fatigue Damage in CFRP-CFRP Adhesive Bonded Joints*, vol. 127. Springer International Publishing, 2021.

[49] “2021_D_Xu_Dynamic feature evaluation onstreaming acoustic emission data foradhesively bonded joints for composite.pdf.” .

[50] J. Manterola, M. Aguirre, J. Zurbitu, J. Renart, A. Turon, and I. Urresti, “Using acoustic emissions (AE) to monitor mode I crack growth in bonded joints,” *Eng. Fract. Mech.*, vol. 224, no. October 2019, p. 106778, 2020.

[51] M. Saeedifar, M. N. Saleh, S. T. De Freitas, and D. Zarouchas, “Damage characterisation of adhesively-bonded Bi-material joints using acoustic emission,” *Compos. Part B Eng.*, vol. 176, no. August, p. 107356, 2019.

[52] M. N. Saleh, M. Saeedifar, D. Zarouchas, and S. T. De Freitas, “Stress analysis of double-lap bi-material joints bonded with thick adhesive,” *Int. J. Adhes. Adhes.*, vol. 97, no. November 2019, p. 102480, 2020.

[53] C. Muir *et al.*, “Damage mechanism identification in composites via machine learning and acoustic emission,” *npj Computational Materials*, vol. 7, no. 1. 2021.

[54] R. Musson, “Intensity and Intensity Scales,” *New Man. Seismol. Obs. Pract. 2*, no. July, pp. 1–41, 2012.

[55] Z. Zhou, R. Cheng, Y. Rui, J. Zhou, and H. Wang, “An Improved Automatic Picking Method for Arrival Time of Acoustic Emission Signals,” *IEEE Access*, vol. 7, pp. 75568–75576, 2019.

[56] F. Sun and B. R. K. Blackman, “Using digital image correlation to automate the measurement of crack length and fracture energy in the mode I testing of structural adhesive joints,” *Eng. Fract. Mech.*, vol. 255, no. June, p. 107957, 2021.

[57] A. Bernasconi, R. A. A. Lima, S. Cardamone, R. B. Campbell, A. H. Slocum, and M. Giglio, “Effect of temperature on cohesive modelling of 3M Scotch-Weld™

7260 B/A epoxy adhesive," *J. Adhes.*, vol. 96, no. 1–4, pp. 437–460, 2020.

[58] "Metallic materials — Verification of static uniaxial testing machines," *ISO 7500-12004*, vol. 2014, p. 13, 2014.

[59] "Determination of the mode I adhesive fracture energy, GIC, of structural adhesives using the double cantilever beam (DCB) and tapered double cantilever beam (TDCB) specimens," *BS ISO 252172009*, 2009.

[60] ASTM International, "Determining the Reproducibility of Acoustic Emission Sensor Response," *ASTM Stand. E976-10*, no. C, pp. 1–7, 2005.

[61] N. HSU and B. FR, "CHARACTERISATION AND CALIBRATION OF ACOUSTIC EMISSION SENSORS," *Charact. CALIBRATION Acoust. Emiss. SENSORS*, 1981.

[62] A. Ruairidh, C. Supervisors, M. G. Droubi, N. Haque, and F. August, "Defect Detection and Condition Assessment of Adhesively-Bonded Joints Using Acoustic Emission," no. August, 2021.

[63] B. A. Behrens, S. Hübner, and K. Wölki, "Acoustic emission—A promising and challenging technique for process monitoring in sheet metal forming," *J. Manuf. Process.*, vol. 29, pp. 281–288, 2017.

[64] A. Boniface, J. Saliba, Z. M. Sbartaï, N. Ranaivomanana, and J. P. Balayssac, "Evaluation of the acoustic emission 3D localisation accuracy for the mechanical damage monitoring in concrete," *Eng. Fract. Mech.*, vol. 223, no. May 2019, p. 106742, 2020.

[65] K. M. Holford *et al.*, "A new methodology for automating acoustic emission detection of metallic fatigue fractures in highly demanding aerospace environments: An overview," *Prog. Aerosp. Sci.*, vol. 90, no. August 2016, pp. 1–11, 2017.

[66] L. Küperkoch, T. Meier, J. Lee, W. Friederich, and E. W. Group, "Automated determination of P-phase arrival times at regional and local distances using higher order statistics," *Geophys. J. Int*, pp. 1159–1170, 2010.

[67] Z. Li and Z. Peng, "An automatic phase picker for local earthquakes with

predetermined locations: Combining a signal-to-noise ratio detector with 1D velocity model inversion," *Seismol. Res. Lett.*, vol. 87, no. 6, pp. 1397–1405, 2016.

[68] F. Sun and B. R. K. Blackman, "A DIC method to determine the Mode I energy release rate G, the J-integral and the traction-separation law simultaneously for adhesive joints," *Eng. Fract. Mech.*, vol. 234, no. December 2019, p. 107097, 2020.

[69] M. Zhu *et al.*, "Digital image correlation assisted characterisation of Mode I fatigue delamination in composites," *Compos. Struct.*, vol. 253, no. November 2019, p. 112746, 2020.

[70] M. G. R. Sause, T. Müller, A. Horoschenkoff, and S. Horn, "Quantification of failure mechanisms in mode-I loading of fiber reinforced plastics utilising acoustic emission analysis," *Compos. Sci. Technol.*, vol. 72, no. 2, pp. 167–174, 2012.

[71] K. Kamiyama, M. Mikuni, T. Matsumoto, S. Matsuda, and H. Kishi, "Crack growth mechanism on SGA adhesive joints," *Int. J. Adhes. Adhes.*, vol. 103, p. 102690, 2020.

[72] D. B. Lee, "Acoustic emission on failure analysis of Rubber-modified epoxy resin," *Fibers Polym.*, vol. 5, no. 4, pp. 259–263, 2004.

[73] S. Huguet, N. Godin, R. Gaertner, L. Salmon, and D. Villard, "Use of acoustic emission to identify damage modes in glass fibre reinforced polyester," *Compos. Sci. Technol.*, vol. 62, no. 10–11, pp. 1433–1444, 2002.